ACS OMEGA

Open Access

http://pubs.acs.org/journal/acsodf

Article

Optimization of Magnetic Behaviors of Au-NP-Decorated MWCNTs and Reduced Graphene Oxide for Biomedical Applications

Sekhar Chandra Ray,* Dilip Kumar Mishra, and Way-Faung Pong*

Cite This: *ACS Omega* 2024, 9, 40067−40074

Read Online

ACCESS | Metrics & More | Article Recommendations | Supporting Information

ABSTRACT: Optimization of electronic/magnetic behaviors of chemically decorated diamagnetic noble-metal gold nanoparticles (Au-NPs ≈5 at. %) on multiwalled carbon nanotubes (MWCNTs) and reduced graphene oxide (r-GO) is studied for future uses of optoelectronic/magnetic and biomedical applications. The changes between Au $4f_{5/2}$ and Au $4f_{7/2}$ ≈ 3.7 eV in X-ray photoelectron spectroscopy and 1.1 (±0.3) eV shifts in the C *K*-edge in X-ray absorption near edge structure spectroscopy confirm that the reduced form of Au^0 was present in the Au-NP-decorated nanocomposites. The potential difference (ΔV) is built due to charge creations at the interface of r-GO/MWCNTs and Au-NPs and shifts in the Fermi level (ΔE_F) due to electronic transfer effects, and as a result, the work functions are reduced from 3.2 eV (MWCNTs) to 3.0 eV (MWCNTs:Au-NPs) and 3.1 (r-GO) to 2.8 eV (r-GO:Au-NPS), respectively. Negligible remanence/coercivity in MWCNTs/r-GO (/Au-NPs) with blocking temperature ≈300 K in MWCNTs:Au-NPs accounted for the existence of diamagnetic Au-NPs in these nanocomposites, which implies a superparamagnetic nature. These results furnish the evidence about the optimization of magnetic behaviors of r-GO/MWCNTs (/Au-NPs) that may possibly be altered as a novel contrast agent for clinical magnetic resonance imaging, drug delivery, and hyperthermia applications.

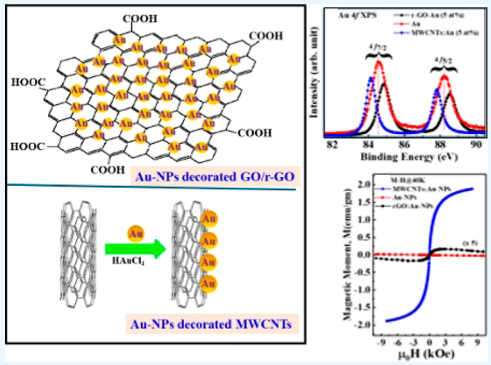

1. INTRODUCTION

Carbon nanomaterials with metal nanoparticles (NPs) supporting heterogeneous materials are popularly investigated because of their engrossing basic properties along with immeasurable prospective applications for the fabrication of various devices, and among them is the magnetic behavior of graphene-based nanomaterials with demanding uses such as nanoscaled magnetic objects.[1−9] Depending upon the nature of metal NPs (dia-/para-/ferro-), these nanocomposites change their electronic/magnetic properties, which are useful for promising potential applications in various areas such as magnetic data recording/storage devices, toners and inks for xerography, magnetic resonance imaging (MRI) contrast agents, and magnetic carriers in the field of biomedicine, e.g., transport of anticancer drugs and heat treatment of cancerous tumors and hyperthermia applications.[6] In particular, the consolidation of diamagnetic Au-NPs and multiwalled carbon nanotubes (MWCNTs)/reduced graphene oxide (r-GO) generates nanohybrid materials[8−10] that have appreciable numerous biomedical usages in biosensors,[1−5,11] gas sensors,[1−5,12] toxicant sensors,[1−5,13] and drug-delivery.[1−5,14,15] The Au-NPs can be attached directly to MWCTNs by chemically linking together with $\pi-\pi$ stacking, hydrophobic, and electrostatic interactions to form a stable nanocomposite structure.[16,17] In the case of r-GO, oxygen surfaces act as reactive sites for bonding of metal NPs and form r-GO:M (Au/Ag) nanocomposites. These materials have their density of states at the Dirac point and/or very near the Dirac point. To enhance the charge carriers, various doping or functionalization techniques involve the transfer of electrons from graphene-based materials to the dopant and vice versa.[13] Most applications need covalent bonds such as chemical oxidation, activation, and liquid-phase reactions of graphene-based materials. This can be achieved by simple attachment/functionalization and/or depositing/doping of Au-NPs on the surface of graphene-based materials. The combination of novel diamagnetic Au-NPs with MWCNTs/r-GO can generate new electronic/magnetic properties that could be used for various optoelectronic/magnetic and biomedicinal applications.[18−20] Synthesis of MWCNTs, however, often uses an Fe catalyst that, to a certain extent, remains as a magnetic impurity that causes unwanted side effects in biomedical applications. To neutralize these ferromagnetic impurities, diamagnetic Au-NPs could be used as a cocatalyst for the fabrication of MWCNTs or further functionalization of MWCNTs for the purposes of favorable magnetic behavior in biomedical applications.

In this work, novel metal-diamagnetic Au-NPs are used for the fabrication of MWCNTs:Au-NPs and r-GO:Au-NPs

Received: June 27, 2024
Revised: August 28, 2024
Accepted: September 2, 2024
Published: September 12, 2024

composites, where Au-NPs are located mainly as an adatom on the r-GO/MWCNTs surfaces by host−guest interactions. This self-assembly and host−guest interactions of Au-NPs and r-GO/MWCNTs change the electronic structure and their magnetic behavior in the nanoscale range for the development of favorable optoelectronic/magnetic device-based technological and biomedical applications.[16,17] Au-NPs can also absorb IR and radio waves and generate heat[18−20] that could also be used for cancer treatment through temperature. On attachment or functionalization of Au-NPs, defects are created that break the symmetry between the graphene sublattices, resulting in the alternation of the magnetic moment. MWCNTs/r-GO (/Au-NPs) are also useful in ultrasound, CT scan, and MRI.[21−,27]

Our motivation is to understand the mechanism to change the electronic structure/bonding performances and hence magnetic behaviors on diamagnetic Au-NP-decorated MWCNTs/r-GO nanocomposite materials. In this case, Au-NPs are located mainly on the r-GO/MWCNTs surfaces by host−guest interactions. This self-assembly and host−guest interactions of Au-NPs and r-GO/MWCNTs impact the crystallite size in influencing the magnetic domain properties of the r-GO/MWCNTs nanocomposite that changes their magnetic behaviors as well as the electronic structure. It is found that the magnetizations are decreased when diamagnetic Au-NPs are decorated with MWCNTs/r-GO. It is also observed that the magnetic behaviors of r-GO:Au-NPs become paramagnetic/superparamagnetic in nature, which are the key to synthesize MWCNTs/r-GO(/Au-NPs) nanocomposites for the favorable usages of optoelectronic/magnetic and biomedical applications, such as novel contrast agents for clinical MRI, biomedicine drug delivery, transport of anticancer drugs, and heat treatment of tumors and hyperthermia.[1−7,21,22,26,27]

2. EXPERIMENTAL DETAILS

MWCNTs are grown by catalytic chemical vapor deposition with an Fe catalyst,[28] whereas r-GO is synthesized by chemical reduction in the modified Hummer method.[29] The MWCNTs/r-GO are chemically decorated with Au-NPs using a $HAuCl_4$ solution for the synthesis of MWCNTs/r-GO (/Au-NPs) composite materials. The "precursor solution Au-NPs" was dropped on MWCNTs/r-GO and dried at ≈70 °C for 10 min and then the "Au" was reduced in Ar^+ plasma ambient at a power of ≈150 W for 15 min under atmospheric pressure. Both nanocomposites MWCNTs/r-GO(/Au-NPs) have ≈5 at. % novel Au-NPs estimated from X-ray photoelectron spectroscopy (XPS) measurement that are given in Table 1. Scanning/transmission electron microscopy (SEM/TEM), Raman spectroscopy, and X-ray diffraction (XRD) characterizations are carried out for surface morphology and micro/crystal structural study, while the change of electronic/bonding behavior is studied using XPS, ultraviolet photoelectron spectroscopy (UPS), and X-ray absorption near edge structure (XANES) spectroscopy. The C *K*-edge and O *K*-edge XANES spectra were obtained using the high-energy spherical grating monochromator 20A-beamline at the National Synchrotron Radiation Research Center (NSRRC), Hsinchu, Taiwan. The magnetizations are studied using a SQUID-type magnetometer. The details of SEM, TEM, XRD, Raman, XPS/UPS, and SQUID measurements are available elsewhere.[29,30]

Table 1. Elemental Composition/Quantification Obtained from XPS and Work Function/Valence Band Maximum (VBM) Obtained from UPS He−I (21.22 eV) Spectra

	composition and quantification			work function (Φ) and VBM from UPS: He−I	
	C (at. %)	O (at. %)	Au (at. %)	W.F.Φ (eV)	VBM (eV)
MWCNTs	95.00	5.00		3.20	4.51
MWCNTs:Au (5 at. %)	91.25	3.79	5	3.18	4.52
rGO	70.00	30.00		3.24	4.30
rGO:Au (5 at. %)	71.14	23.99	5	2.85	4.10

3. RESULTS AND DISCUSSION

The surface morphology and microstructures of MWCNTs, r-GO, and MWCNTs/r-GO (/Au-NPs) are studied using SEM, TEM, XRD, and Raman spectroscopy. Figure 1a,b shows the SEM of MWCNTs/r-GO and the embedded TEM of MWCNTs/r-GO (/Au-NPs). The results show that the nanotubes and r-GOs are formed with graphite particles along with a uniform decoration of Au-NPs throughout the MWCNTs/r-GO surfaces. The XRD spectra of MWCNTs/MWCNTs: Au-NPs and r-GO/r-GO:Au-NPS are shown in Figure 1c. Typical diffraction peaks (plane) of MWCNT/r-GO are observed at $2\theta \approx 26.1°$ (002) and 43.3° (100), respectively, assigned as graphite planes with a hexagonal structure.[31−33] Other peaks at 2θ values of ≈12° (001), ≈38° (111), ≈44° (200), and ≈65° (220) are observed. After decoration of Au-NPs on MWCNTs/r-GO surfaces, the diffraction peaks are slightly shifted at higher/lower 2θ-angle sides in MWCNTs/r-G(/Au-NPs) nanocomposites due to the exchange of atoms/electrons in the composites. The wide peak of the (002) plane with slight shifts in higher angles ($\Delta\theta \approx 1.10°$) with an extra peak at $2\theta = 38.3°$ is observed in r-GO that comes from the graphitic surface. The average particle size was ≈2.5 and 2.7 nm for MWCNTs and r-GO, respectively, which are obtained using the Scherrer equation: $L = K\lambda/(\beta \cos\theta)$ ($K = 0.89$, $\lambda = 1.5406$ Å, β = width of diffraction line, and θ = peak angle).[34] The Raman spectra of MWCNTs/MWCNTs:Au-NPs and r-GO/r-GO:Au-NPs are shown in Figure 1d,e. The Raman spectrum of MWCNTs (r-GO) displays three characteristic peaks: D band at ≈1329.3 cm^{-1}(≈1344.5 cm^{-1}) ascribed to the out-of-plane breathing mode of the sp^2 atom due to defects; G band at ≈1582.8 cm^{-1}(≈1577.8 cm^{-1}), the E_{2g} phonons at the center of the Brillion zone; and 2D band at ≈2653.5 cm^{-1} (≈2681.5 cm^{-1}), the second order of the D band. On the decoration of Au-NPs, these three peaks of MWCNTs:Au-NPs (r-GO:Au-NPs) are shifted to ≈1329.3 → 1320.9 cm^{-1} (≈1344.5 →1335.3 cm^{-1}), ≈1582.8 →1564.4 cm^{-1} (≈1577.8 →1585.2 cm^{-1}), and ≈2653.5 →2642.8 cm^{-1} (≈2681.5 →2656.9 cm^{-1}), respectively.[35−37] The peaks of MWCNTs (r-GO) arise at ≈2911.1 cm^{-1} (2953.5 cm^{-1}) via combination of the (D + G) band that are shifted to ≈2898.9 cm^{-1} (2934.0 cm^{-1}), respectively, for the Au-NPs and MWCNTs:Au-NPs/r-GO:Au-NPs nanocomposites. The other extra peak that arises in MWCNTs (MWCNTs:Au-NPs) at ≈3200 $cm^{-1}$is the 2G peak. The D peak is also considered as a defect-activated signature via the interval double resonance process and its intensity provides the amount of disorder of the nanocomposites.[30,33−40] Peak shifts are due to the change in charge density due to Au-NP decoration on the surface of MWCNTs (r-GO).[41,42] In addition, a shoulder-like peak was also observed in MWCNTs

https://doi.org/10.1021/acsomega.4c05962
ACS Omega 2024, 9, 40067−40074

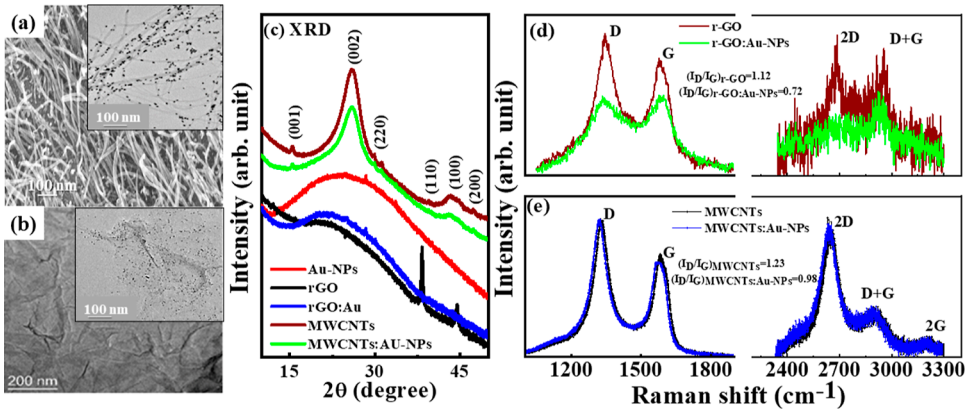

Figure 1. (a) SEM image of MWCNTs and embedded TEM image of MWCNTs:Au-NPs (5 at. %) and (b) SEM image of r-GO and embedded TEM image of r-GO:Au-NPs (5 at. %). (c) XRD spectra of MWCNTs, MWCNTs:Au (5 at. %), Au-NPs, r-GO, and r-GO:Au (5 at. %). Raman spectra of (d) r-GO and r-GO-AuNPs (5 at. %) and (e) MWCNTs and MWCNTs:AuNPs (5 at. %).

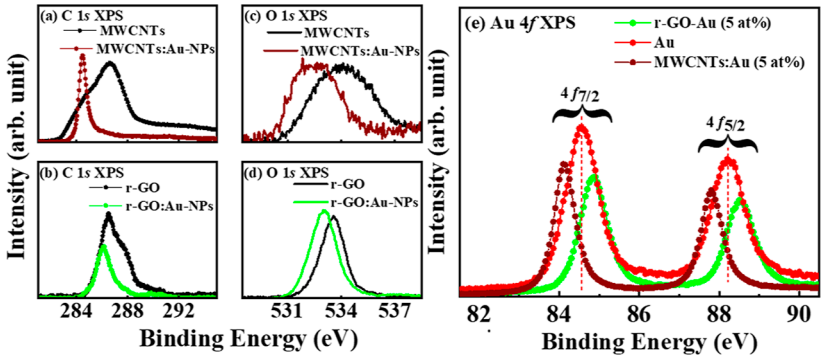

Figure 2. (a) C 1s XPS spectra of MWCNTs and MWCNTs:AuNPs (5 at. %), (b) C 1s XPS spectra of r-GO and r-GO:AuNPs (5 at. %), (c) O 1s XPS spectra of MWCNTs and MWCNTs:AuNP (5 at. %), (d) O 1s XPS spectra of r-GO and r-GO:AuNP (5 at. %), and (e) high-resolution Au 4f XPS spectra of MWCNTs:AuNPs (5 at. %) and r-GO-AuNP (5 at. %) along with Au-NPs as a reference.

(MWCNTs:Au-NPs)/r-GO (r-GO:Au-NPs) at ≈1610 cm^{-1} (1601 cm^{-1})/1623 cm^{-1} (1627 cm^{-1}), known as the defect-generated (disordered) band on MWCNTs/r-GO (/Au-NPs) surfaces. Peak shifts and intensity variations indicate significant structural disorders due to the decoration of Au-NPs on MWCNTs (r-GO). The intensity ratio of the D and G bands I_D/I_G gives an insight into the reduction process by the electronic transfer effects at the interface in between MWCNTs (r-GO) and Au-NPs. I_D/I_G ratio changes: 1.23 → 0.98 (1.12 → 0.72) for MWCNTs→ MWCNTs:Au-NPs (r-GO → r-GO:Au-NPs). The decrease of I_D/I_G implies an increase in the L_a, the sp^2 crystallite size that indicates destruction of the sp^2 C═C bonds in the structural matrix[38] on Au-NP decoration on the surface of MWCNT/r-GO.[23−25,40]

The elemental and quantification analyses of MWCNTs, r-GO, and MWCNTs/r-GO (Au-NPs) were investigated using XPS analysis. Figure S1 in Supporting Information shows the XPS survey spectra, where it is observed that the C 1s, O 1s, and Au-4f/4d peaks are present in the respective materials, indicating the presence of C, O, and Au atoms in the nanocomposites MWCNT/r-GO (/Au-NPs). Elemental and quantification analysis shows that the presence of Au-NPs (≈5 at. %) in both MWCNTs/r-GO (/Au-NPs) implies the formation of MWCNTs/r-GO(/Au-NPs) composites. The detailed elemental compositions and quantification analysis are tabulated in 1. Figure 2a−d shows the XPS spectra C 1s and O 1s of MWCNTs, r-GO, and MWCNTs/r-GO (/Au-NPs), where it is observed that the peak intensities changed and their peak positions shifted. Figure 2e shows the Au 4f core-level XPS spectra of MWCNTs/r-GO (/Au-NPs) along with Au-NPs. The Au 4f doublet band of Au-NPs has binding energies of 84.55 and 88.25 eV, corresponding to Au $4f_{5/2}$ and Au $4f_{7/2}$ peaks, respectively.[39] These double band peaks are shifted at a lower (higher) energy band for the MWCNTs:Au-NPs (r-GO:Au-NPs) → 84.1 eV (84.8 eV) and 87.8 eV (88.5 eV), respectively. The difference in the chemical shift between Au $4f_{5/2}$ and Au $4f_{7/2}$ peaks for Au-NPs and MWCNTs:Au-NPs (r-GO:Au-NPs) is ≈ 3.7 eV that confirms the reduced form of Au^0 in MWCNTs/r-GO(/Au-NPs) nanocomposites.[43−45] The details of the electronic and bonding structures were also studied using the deconvoluted spectrum of C 1s and O 1s XPS spectra as shown in Figure S2a,b and the deconvoluted results are tabulated in Table S1. The C 1s spectrum is the signature of sp^2 C═C, O−H/O−C−O, and C═O, respectively, while the O 1s spectrum is the signature of C═O, C−O, and phenolic groups, respectively.[29,46,47] In the decoration of Au-NPs, the peaks of different species bonded to C−/O− shifted with their intensities changes due to substitute the vacancies in sp^2 sites, formation of defects and M−O/M−C bonds in the structure of the nanocomposites structure.[19,47]

The C *K*-edge and O *K*-edge XANES spectra of MWCNTs/r-GO and MWCNTs/r-GO (/Au-NPs) along with HOPG as a reference are shown in Figure 3a,b. In graphene-based materials, the C *K*-edge XANES spectra are divided into three regions: (i) the $\pi^*_{C=C(sp^2)}$ resonance at ≈285 ± 1 eV,

https://doi.org/10.1021/acsomega.4c05962
ACS Omega 2024, 9, 40067−40074

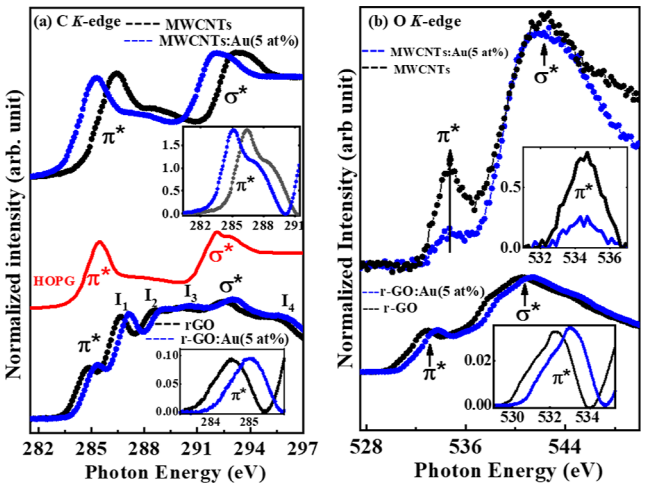

Figure 3. (a) C *K*-edge and (b) O *K*-edge XANES spectra of MWCNTs and MWCNTs:AuNPs (5 at. %) and r-GO and r-GO-AuNP (5 at. %) along with the C *K*-edge spectrum of HOPG as a reference.

(ii) C−H* resonance ≈288 ± 1 eV, and (iii) the region ≈290−315 eV corresponding to σ^* resonance. These resonances serve as a fingerprint of sp^2-hybridized C−C bonds and C−H bonds, respectively.[41] In C *K*-edge XANES, as shown in Figure 3a, the characteristic features of MWCNTs (r-GO) at ∼285.0 eV (284.8 eV) and ∼293.5 eV (292.5 eV) are described as the unoccupied 1s → π^* and 1s → σ^* state transitions, respectively.[48] The spectral features for MWCNTs/r-GO(/Au-NPs) are similar to those of MWCNTs (r-GO); the absorption edges are shifted toward the lower (higher) energy level for MWCNTs:Au-NPs (r-GO:Au-NPs) and are clearly observed in Figure 3a. The 1s → π^* and 1s → σ^* state transitions could be compared with the reference HOPG, where these transitions are observed at ≈285.5 and 292.1 eV, respectively. This shift (change) in the absorption edge of MWCNTs/r-GO(/Au-NPs) is due to change of the band gap and the work function due to the structural rearrangement via the attachment of Au-NPs.[29] It is also possible that defects are created by the decoration of Au-NPs on the MWCNT (r-GO) surfaces. Apart from π^* and σ^* resonance peaks, a wide peak within the range of ≈287.8−289.0 eV is observed in MWCNTs (MWCNTs:Au-NPs) and is known as the signatures of C−H bonds and interlayer graphite states, respectively, whereas in r-GO (r-GO:Au-NPs), three prominent resonances are observed. The resonance at ≈286.6 (286.7) eV (I_1) and ≈290.1(290.6) eV (I_3) is assigned to π^* (C═O/COOH) and π^* (COOH), respectively, whereas the resonance ≈288.0 (289.1) eV (I_2) is the signature of few-layer graphene.[49] The literature evidence for the feature (∼289 eV) originates from −COOH moieties present in r-GO.[50] The resonance above σ^* at ≈295.0 (295.6) eV (I_4) is assigned as C═O moieties.[51] The *K*-edge XANES spectra are shown in Figure 3b, where the $\pi^*_{C=O}$ features of MWCNTs (r-GO) and MWCNTs/r-GO (/Au-NPs) are observed at ≈534.7 eV (532.8 eV) and 534.5 eV (533.5 eV), respectively, and the $\sigma^*_{C=O}$ features are observed at ≈542.5 eV (540.4 eV) and 542.7 eV (541.2 eV), respectively.[49,52] The change of π^* intensity in O *K*-edge XANES spectra implies the Au-NPs bound with oxygen, which is consistent with the $I_D/I_{G\ ratio}$ obtained from the Raman spectra indicating the formation of nanocomposites MWCNTs/r-GO (/Au-NPs). Peak shift and intensity variations of both the π^* and σ^* states of MWCNTs (r-GO) and MWCNTs/r-GO (/Au-NPs) in C *K*-edge and O *K*-edge XANES spectra indicate that structural changes/modifications occur on the decoration of Au-NPs without disturbing the pristine MWCNTs/r-GO structure.

The M−H hysteresis curves of MWCNTs (MWCNTs:Au-NPs) and r-GO (r-GO:Au-NPs) together with Au-NPs were measured at low temperature ≈40K within the range of ±9.0 kOe and are shown in Figure 4 (a,b). From the spectral

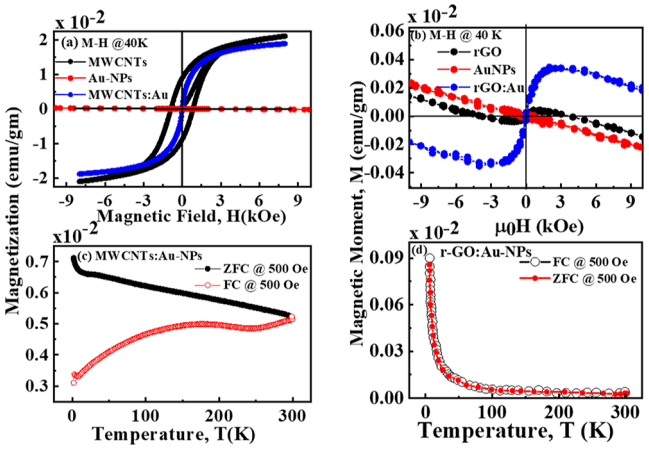

Figure 4. M−H hysteresis loops of (a) MWCNTs and MWCNTs:AuNPs (5 at. %) and (b) r-GO and r-GO:AuNP (5 at. %) along with AuNPs as a reference. M−T curve of (c) MWCNTs and MWCNTs:AuNPs (5 at. %) and (d) r-GO and r-GO:AuNP (5 at. %).

features, it is observed that the highest magnetization is in MWCNTs, while others (r-GO, r-GO:Au-NPs, and MWCNTs:Au) show more confined hysteretic features and a lower saturation of magnetization. On the decoration of noble Au-NP metal on MWCNTs/r-GO, the magnetizations are reduced in MWCNTs:Au-NPs drastically, but the magnetization of r-GO:Au-NPs is slightly enhanced compared to pristine r-GO but negligible in comparison to MWCNTs(/Au-NPs). The decrease in saturation magnetization of MWCNTs:Au-NPs can be accounted for by the existence of diamagnetic Au-NPs. The magnetization of pure Au-NPs is ferromagnetic/diamagnetic depending on the sizes (smaller/larger) of the particle.[53] The observed magnetism in the MWCNTs/r-GO(/Au-NPs) is due to the creation of defects and/or vacancies during diamagnetic-Au-NP decoration. The attachment of Au-NPs, formation of possible Au−C−O/C−Au−O bonds, and reduction of C═C sp^2 atoms in the MWCNTs/r-GO(/Au-NPs) are in good agreement with the edge shifts in XANES as well as decreases of I_D/I_G ratio in the Raman spectra, which are responsible for change in their magnetization. Defects in MWCNTs/r-GO(/Au-NPs) break the translational symmetry of the lattice and create localized states at the Fermi energy. Most of the theoretical/experimental work[54−57] finds that the net spin is stable because of the huge p conjugation and long-range orderly magnetic coupling. We believe that the room/below-room-temperature ferromagnetism is an intrinsic property of graphene-based nanocomposite materials. The magnetization curve shows negligible (or much less) magnitude of remanence/coercivity of MWCNTs/r-GO(/Au-NPs) nanocomposites are paramagnetic/superparamagnetic in nature.[52]

https://doi.org/10.1021/acsomega.4c05962
ACS Omega 2024, 9, 40067−40074

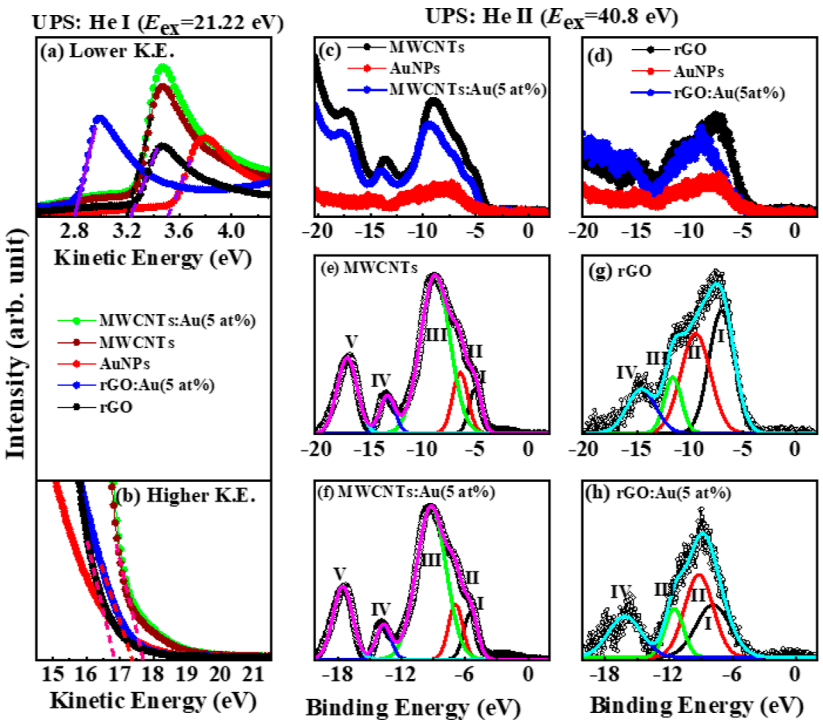

Figure 5. UPS He−I (E_{ex} = 21.22 eV) spectra of MWCNTs and MWCNTs:AuNPs (5 at. %), r-GO and r-GO-AuNP (5 at. %), and Au-NPs: (a) low energy state for determination of the work function and (b) higher energy state for determination of the VBM of these materials. UPS He−II spectra of (c−e) MWCNTs and MWCNTs:AuNPs (5 at. %) and their deconvolution and (f−h) r-GO and r-GO-AuNP (5 at. %) and their deconvolution along with AuNPs as a reference.

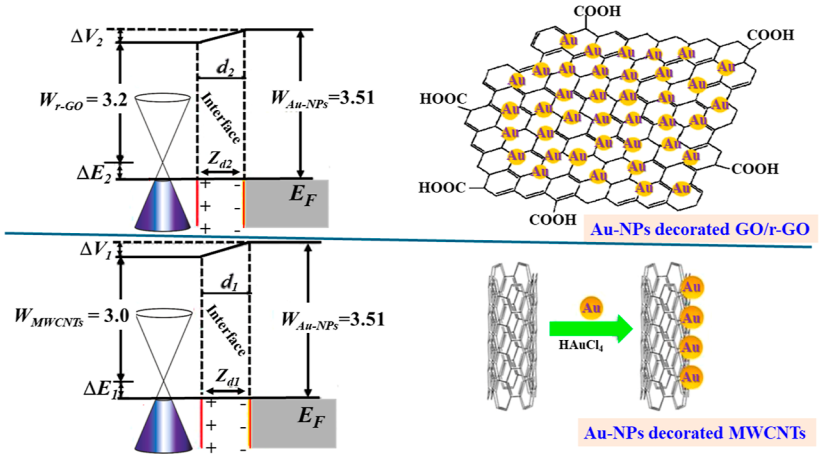

Figure 6. Schematic energy band diagram of the r-GO:AuNPs/MWCNTs:AuNPs interface and consequential common Fermi level.

The magnetism of r-GO and r-GO:Au-NPs shows almost similar saturation magnetization and is paramagnetic/superparamagnetic in nature, suggesting the impact of the crystallite size in influencing the magnetic domain properties of the r-GO nanocomposite. The temperature dependence of zero field cooled (ZFC) and FC DC magnetization of MWCNTs/r-GO(/Au-NPs), measured at the external magnetic field of 500 Oe, is shown in Figure 4c,d. The semi- λ nature of FC/ZFC curve observed in MWCNTs:Au-NPs shows a maximum difference at the blocking temperature $T_B \approx 300$ K that implies and confirms the superparamagnetic nature.[58] These results provide evidence regarding the optimization of the magnetic properties of r-GO/MWCNTs (/Au-NPs), which could possibly alter drug delivery and hyperthermia and act as a novel contrast agent for clinical MRI applications.

To obtain more information on Au-NP decoration in the MWCNTs/r-GO nanocomposite, we studied VB DOS near E_F by carrying UPS measurements in He−I ($h\nu$ = 21.22 eV) and He−II ($h\nu$ = 40.81 eV) radiation as shown in Figure 5a−d. We have estimated the work functions (Φ)/VBM from the intersection of the slope of each spectrum on the lower/higher K.E. side of the UPS He−I spectra as shown in Figure 5a,b and their values are tabulated in Table 1. It is found that the Φ/VBM are reduced as follows: Φ/VBM ⇒ 3.20 eV/4.52 eV (MWCNTs) → 3.17 eV/4.49 eV (MWCNTs:Au-NPs) and 3.24 eV/4.30 eV (r-GO) → 2.85 eV/4.09 eV (r-GO:Au-NPs). The VBM shift in the quasi-localized states at the Fermi level creates a defect in the graphene-based lattice that cause a change in their magnetism.[59] From Figure 5b, a small shift of MWCNTs/r-GO(/Au-NPs) toward the Fermi edge (green/

https://doi.org/10.1021/acsomega.4c05962
ACS Omega 2024, 9, 40067−40074

blue line) increases in the DOS compared to MWCNTs/r-GO that affects their magnetism as shown in Figure 4a,b. An increase in DOS enhances the sp^2 C−C cluster along with the formation of new different C−/O−-related bonds as discussed in the XPS results (see S1). Variation of Φ and VBM is related to the dipole moment. The difference in Φ (≈0.21 eV) implies a reduction in the dipole moment, which has an impact on the redistribution of the charge. Charge redistribution gives rise to unpaired electrons (vacancies) that eventually influence the magnetization of MWCNTs/r-GO nanocomposites.[60] The UPS spectra corresponding to the VB DOS of MWCNTs/r-GO and MWCNTs/r-GO(/Au-NPs) nanocomposites obtained under He−II radiation are shown in Figure 5c,d. We have deconvoluted the spectra into five/four Gaussian lines for MWCNTs(/Au-NPs)/r-GO(/Au-NPs) within the binding energy range of ≈0−20 eV[61] as shown in Figure 5e−h. The deconvoluted Gaussian lines of the MWCNTs/r-GO(/Au-NPs) nanocomposite are assigned as the C $2p_\pi$ (5.2 ± 0.1 eV), $2p_{(\pi-\sigma)}$ overlap state (7.0 ± 0.3 eV), C $2p_\sigma$ (8.8 ± 0.3 eV), C 2sp mixed state (11.4 ± 0.4 eV), C 2s (13 eV), and O 2s (>16 eV).[62−64] However, some researchers have reported that the peaks at ∼13.25 and 11.78 eV are due to σ and π bonds arising from C═O and the O-lone pair bonds, respectively.[65,66] The different parameters of the deconvoluted UPS He−II spectra are listed in Table S2.

The noble Au-NP-decorated MWCNTs/r-GO induces p doping[67] known as "percolation", which is the opening up of conducting channels through the interface in between Au-NPs and MWCNTs/r-GO and grain boundaries.[68] In Figure 6, the Φ of r-GO/MWCNTs (/Au-NPs) and Au-NPs and their effects of charge transfer on Fermi-level shifts are indicated. The Φ of r-GO:Au-NPs ≈2.80 eV, MWCNTs:Au-NPs ≈3.0 eV, and Au-NPs ≈3.51 eV are, respectively, indicated by $W_{rGO:Au-NPs}$, $W_{MWCNTs:Au-NPs}$, and W_{Au-NPs}. On decoration of Au-NPs on MWCNTs/r-GO, a self-assembly and host−guest interactions with noncovalent forces between r-GO/MWCNTs and Au-NPs occur and a small potential difference (ΔV) is built that creates charges at the interface of r-GO/MWCNTs and Au-NPs. The Fermi level E_F of the r-GO/MWCNTs:Au-NPs energy bands shifts in the presence of the metal dopant by ΔE_F. It is believed that the decrease in work function of r-GO/MWCNTs (/Au-NPs) is due to the incorporation of Au-NPs into the r-GO/MWCNTs, which indicates a change in the surface potential, and is due to pure electronic transfer effects in Au-NPs. Since the Φ of Au (3.51 eV) is higher than that of r-GO/MWCNTs (3.2/3.0 eV), electron transfer occurs automatically at the interface within the Au-NPs/(r-GO/MWCNTs) hybrid structure. This would effectively dope r-GO/MWCNTs with more electrons and reduce their Fermi level below the conical point, as shown in Figure 6. These results imply that the r-GO/MWCNTs are properly decorated with Au-NPs through self-assembly and host−guest interactions of Au-NPs and r-GO/MWCNTs. This is the key role for the formation of composite materials that changes the electronic structure and their magnetic behaviors, particularly the formation of para/superparamagnetic materials that could be useful for biomedical applications.

4. CONCLUSIONS

Our investigation shows that the Au-NPs are responsible for the change of the magnetic nature of MWCNTs/r-GO(/Au-NPs) nanocomposites. The carbon nanomaterials functionalized with Au-NPs are nontoxic and inactive in chemical reactions, have the ability to coexist with living tissues or organisms without causing harm, and show antimicrobial behaviors, which means that they possess the ability to control/manipulate/optimize the structural behavior of MWCNTs/r-GO(/Au-NPs) which opens new vistas for electronic/magnetic and biomedical applications, particularly, the formation of para/superparamagnetic materials could be useful *in* drug delivery, hyperthermia, and novel contrast agents of clinical MRI.

■ ASSOCIATED CONTENT

Supporting Information

The Supporting Information is available free of charge at https://pubs.acs.org/doi/10.1021/acsomega.4c05962.

XPS survey spectra of MWCNTs, r-GO, MWCNTs:Au (5 at. %), and r-GO:Au (5 at. %) and convoluted C 1s and O 1s XPS spectra of MWCNTs, r-GO, MWCNTs:Au (5 at. %), and r-GO:Au (5 at. %) into different peaks along with their results in tabulated form (PDF)

■ AUTHOR INFORMATION

Corresponding Authors

Sekhar Chandra Ray − *Department of Physics, Faculty of Engineering and Technology (ITER), Siksha "O" Anusandhan Deemed to be University, Bhubaneswar 751 030 Odisha, India; Department of Physics, CSET, University of South Africa, Florida 1710 Johannesburg, South Africa; Department of Physics, Tamkang University, Taipei 251, Taiwan;* orcid.org/0000-0003-3202-4739; Email: sekharchandraray@gmail.com

Way-Faung Pong − *Department of Physics, Tamkang University, Taipei 251, Taiwan*; Email: wfpong@mail.tku.edu.tw

Author

Dilip Kumar Mishra − *Department of Physics, Faculty of Engineering and Technology (ITER), Siksha "O" Anusandhan Deemed to be University, Bhubaneswar 751 030 Odisha, India*

Complete contact information is available at: https://pubs.acs.org/10.1021/acsomega.4c05962

Notes

The authors declare no competing financial interest.

■ ACKNOWLEDGMENTS

The W.F.P. thanks the Ministry of Science and Technology (MoST) of Taiwan for providing financial support for research under the projects MoST 112-2112-M-032-009-MY2 and 112-2112-M- 032-014. S.C.R. gratefully acknowledges the NSTC, Taiwan, for providing financial support for research under the project NSTC 113-2811-M-032-001.

■ REFERENCES

(1) Hassan, F.; Tang, Y.; Bisoyi, H. K.; Li, Q. Photochromic Carbon Nanomaterials: An Emerging Class of Light-Driven Hybrid Functional Materials. *Adv. Mater.* **2024**, *36* (32), 2401912.

(2) Yuan, Z.; Xiao, X.; Li, J.; Zhao, Z.; Yu, D.; Li, Q. Self-Assembled Graphene-Based Architectures and Their Applications. *Adv. Sci.* **2018**, *5* (2), 1700626.

(3) Tang, Y.; Wang, X.; Chen, S.; Li, Q. Photoactivated theranostic nanomaterials based on aggregation- induced emission luminogens for

cancer photoimmunotherapy. *Responsive Mater.* **2024**, *2* (2), No. e20240003.
(4) Zhang, Z.; Hu, Z.; Xing, J.; Li, Q. Transient and elusive intermediate states in self-assembly processes: An overview. *Responsive Mater.* **2024**, *2* (2), No. e20240009.
(5) Wang, X.; Sprinkle, B.; Bisoyi, H. K.; Yang, T.; Chen, L.; Huang, S.; Li, Q. Colloidal tubular microrobots for cargo transport and compression. *PANS* **2023**, *120* (37), No. e2304685120.
(6) Vyalikh, A.; Wolter, A. U. B.; Hampel, S.; Haase, D.; Ritschel, M.; Leonhardt, A.; Grafe, H. J.; Taylor, A.; Krämer, K.; Büchner, B.; Klingeler, R. A carbon-wrapped nanoscaled thermometer for temperature control in biological environments. *Nanomedicine* **2008**, *3*, 321−327.
(7) Tyagi, P. K.; Misra, A.; Singh, M. K.; Misra, D. S.; Ghatak, J.; Satyam, P. V.; Le Normand, F. High-resolution transmission electron microscopy mapping of nickel and cobalt single-crystalline nanorods inside multiwalled carbon nanotubes and chirality calculations. *Appl. Phys. Lett.* **2005**, *86* (25), 253110−253112.
(8) Segura, R. A.; Contreras, C.; Henriquez, R.; Häberle, P.; Acuña, J. J. S.; Adrian, A.; Alvarez, P.; Hevia, S. A. Gold nanoparticles grown inside carbon nanotubes: synthesis and electrical transport measurements. *Nanoscale Res. Lett.* **2014**, *9* (1), 207−213.
(9) Ahmad, R.; Griffete, N.; Lamouri, A.; Felidj, N.; Chehimi, M. M.; Mangeney, C. Nanocomposites of Gold Nanoparticles@ Molecularly Imprinted Polymers: Chemistry, Processing, and Applications in Sensors. *Chem. Mater.* **2015**, *27*, 5464−5478.
(10) Ou, Y. Y.; Huang, M. H. High-Density Assembly of Gold Nanoparticles on Multiwalled Carbon Nanotubes Using 1-Pyrenemethylamine as Interlinker. *J. Phys. Chem. B* **2006**, *110*, 2031−2036.
(11) Tîlmaciu, C. M.; Morris, M. C. Carbon nanotube biosensors. *Front. Chem.* **2015**, *3*, 59.
(12) Zanolli, Z.; Leghrib, R.; Felten, A.; Pireaux, J. J.; Llobet, E.; Charlier, J. C. Gas Sensing with Au-Decorated Carbon Nanotubes. *ACS Nano* **2011**, *5*, 4592−4599.
(13) Saha, K.; Agasti, S. S.; Kim, C.; Li, X.; Rotello, V. M. Gold Nanoparticles in Chemical and Biological Sensing. *Chem. Rev.* **2012**, *112*, 2739−2779.
(14) Sainsbury, T.; Stolarczyk, J.; Fitzmaurice, D. An Experimental and Theoretical Study of the Self-Assembly of Gold Nanoparticles at the Surface of Functionalized Multiwalled Carbon Nanotubes. *J. Phys. Chem. B* **2005**, *109*, 16310−16325.
(15) Fási, A.; Pálinkó, I.; Seo, J. W.; Konya, Z.; Hernadi, K.; Kiricsi, I. Sonication assisted gold deposition on multiwall carbon nanotubes. *Chem. Phys. Lett.* **2003**, *372*, 848−852.
(16) Tasis, D.; Tagmatarchis, N.; Bianco, A.; Prato, M. Chemistry of Carbon Nanotubes. *Chem. Rev.* **2006**, *106*, 1105−1136.
(17) Chu, A.; Cook, J.; Heesom, R. J. R.; Hutchison, J. L.; Green, M. L. H.; Sloan, J. Filling of Carbon Nanotubes with Silver, Gold, and Gold Chloride. *Chem. Mater.* **1996**, *8*, 2751−2754.
(18) Bae, S.; Kim, H.; Lee, Y.; Xu, X.; Park, J.-S.; Zheng, Y.; Balakrishnan, J.; Lei, T.; Ri Kim, H.; Song, Y. I.; Kim, Y.-J.; Kim, K. S.; Özyilmaz, B.; Ahn, J.-H.; Hong, B. H.; Iijima, S. Roll-to-roll production of 30-inch graphene films for transparent electrodes. *Nat. Nanotechnol.* **2010**, *5*, 574−578.
(19) Zhou, X.; Liang, F. Application of graphene/graphene oxide in biomedicine and biotechnology. *Curr. Med. Chem.* **2014**, *21*, 855−869.
(20) Romero-Aburto, R.; Narayanan, T. N.; Nagaoka, Y.; Hasumura, T.; Mitcham, T. M.; Fukuda, T.; Cox, P. J.; Bouchard, R. R.; Maekawa, T.; Kumar, D. S.; Torti, S. V.; Mani, S. A.; Ajayan, P. M. Fluorinated graphene oxide; a new multimodal material for biological applications. *Adv. Mater.* **2013**, *25*, 5632−5637.
(21) Yazyev, O. V. Emergence of magnetism in graphene materials and nanostructures. *Rep. Prog. Phys.* **2010**, *73*, 056501.
(22) Stoneham, M. The strange magnetism of oxides and carbons. *J. Phys.: Condens. Matter* **2010**, *22*, 074211.
(23) Hainfeld, J. F.; Lin, L.; Slatkin, D. N.; Avraham Dilmanian, F.; Vadas, T. M.; Smilowitz, H. M. Gold nanoparticle hyperthermia reduces radiotherapy dose. *Nanomedicine* **2014**, *10*, 1609−1617.
(24) Collins, C.; McCoy, R.; Ackerson, B.; Collins, G.; Ackerson, C. Radiofrequency heatingpathways for gold nanoparticles. *Nanoscale* **2014**, *6* (15), 8459−8472.
(25) Nordebo, S.; Dalarsson, M.; Ivanenko, Y.; Sjöberg, D.; Bayford, R. On the physical limitations forradio frequency absorption in gold nanoparticle suspensions. *J. Phys. D: Appl. Phys.* **2017**, *50*, 155401.
(26) Kim, J.; Chhour, P.; Hsu, J.; Litt, H. I.; Ferrari, V. A.; Popovtzer, R.; Cormode, D. P. Use ofnanoparticle contrast agents for cell tracking with computed tomography. *Bioconjugate Chem.* **2017**, *28*, 1581−1597.
(27) Lee, N.; Choi, S. H.; Hyeon, T. Nano-sized CT contrast agents. *Adv. Mater.* **2013**, *25*, 2641−2660.
(28) Musso, S.; Porro, S.; Giorcelli, M.; Chiodoni, A.; Ricciardi, C.; Tagliaferro, A. Macroscopic growth of carbon nanotube mats and their mechanical properties. *Carbon* **2007**, *45*, 1133−1136.
(29) Idisi, D. O.; Ali, H.; Oke, J. A.; Sarma, S.; Moloi, S. J.; Ray, S. C.; Wang, H. T.; Jana, N. R.; Pong, W. F.; Strydom, A. M. Electronic, electrical and magnetic behaviours of reduced graphene-oxide functionalized with silica coated gold nanoparticles. *Appl. Surf. Sci.* **2019**, *483*, 106−113.
(30) Ray, S. C.; Pao, C. W.; Tsai, H. M.; Chiou, J. W.; Pong, W. F.; Chen, C. W.; Tsai, M.-H.; Papakonstantinou, P.; Chen, L. C.; Chen, K. H. A comparative study of the electronic structures of oxygen- and chlorine-treated nitrogenated carbon nanotubes by x-ray absorption and scanning photoelectron microscopy. *Appl. Phys. Lett.* **2007**, *91* (20), 1−3.
(31) Kuila, T.; Bose, S.; Mishra, A. K.; Khanra, P.; Kim, N. H.; Lee, J. H. Chemical functionalization of graphene and its applications. *Prog. Mater. Sci.* **2012**, *57*, 1061−1105.
(32) Zhao, J.; Hu, W.; Li, H.; Ji, M.; Zhao, C.; Wang, Z.; Hu, H. One-step green synthesis of a ruthenium/graphene composite as a highly efficient catalyst. *RSC Adv.* **2015**, *5*, 7679−7686.
(33) Over, H. Ruthenium dioxide, a fascinating material for atomic scale surface chemistry. *Appl. Phys. A: Mater. Sci. Process.* **2002**, *75*, 37−44.
(34) Cullity, B. D.; Stock, S. R. *Elements of X-Ray Diffraction*; Pearson: New International ed.: UK, 2001.
(35) Ferrari, A. C.; Meyer, J. C.; Scardaci, V.; Casiraghi, C.; Lazzeri, M.; Mauri, F.; Piscanec, S.; Jiang, D.; Novoselov, K. S.; Roth, S.; Geim, A. K. Raman Spectrum of Graphene and Graphene Layers. *Phys. Rev. Lett.* **2006**, *97*, 187401.
(36) Claramunt, S.; Varea, A.; López-Díaz, D.; Velázquez, M. M.; Cornet, A.; Cirera, A. The Importance of Interbands on the Interpretation of the RamanSpectrum of Graphene Oxide. *J. Phys. Chem. C* **2015**, *119*, 10123−10129.
(37) Idisi, D. O.; Oke, J. A.; Benecha, E. M.; Moloi, S. J.; Ray, S. C. Magnetic properties of graphene oxide functionalized with "Au" and "Fe_2O_3" nanoparticles: A comparative study. *Mater. Today Proc.* **2021**, *44*, 5037−5043.
(38) Tuinstra, F.; Koenig, J. L. Raman Spectrum of Graphite. *J. Chem. Phys.* **1970**, *53*, 1126−1130.
(39) Ferrari, A. C. Raman spectroscopy of graphene and graphite: Disorder, electron-phonon coupling, doping and nonadiabatic effects. *Solid State Commun.* **2007**, *143*, 47−57.
(40) Ferrari, A. C.; Robertson, J. Interpretation of Raman spectra of disordered and amorphous carbon. *Phys. Rev. B* **2000**, *61*, 14095−14107.
(41) Ryu, S.; Han, M. Y.; Maultzsch, J.; Heinz, T. F.; Kim, P.; Steigerwald, M. L.; Brus, L. E. Reversible Basal Plane Hydrogenation of Graphene. *Nano Lett.* **2008**, *8*, 4597−4602.
(42) Graf, D.; Molitor, F.; Ensslin, K.; Stampfer, C.; Jungen, A.; Hierold, C.; Wirtz, L. Spatially Resolved Raman Spectroscopy of Single- and Few-Layer Graphene. *Nano Lett.* **2007**, *7*, 238−242.
(43) Kim, S. S.; Kim, Y. R.; Chung, T. D.; Sohn, B. H. Tunable Decoration of Reduced Graphene Oxide with Au Nanoparticles for the Oxygen Reduction Reaction. *Adv. Funct. Mater.* **2014**, *24*, 2764−2771.
(44) Behera, M.; Ram, S. Inquiring the mechanism of formation, encapsulation, and stabilization of gold nanoparticles by poly (vinyl

https://doi.org/10.1021/acsomega.4c05962
ACS Omega 2024, 9, 40067−40074

pyrrolidone) molecules in 1-butanol. *Appl. Nanosci.* **2014**, *4*, 247−254.
(45) Abyaneh, M. K.; Paramanik, D.; Varma, S.; Gosavi, S. W.; Kulkarni, S. K. Formation of gold nanoparticles in polymethylmethacrylate by UV irradiation. *J. Phys. D Appl. Phys.* **2007**, *40*, 3771−3779.
(46) Ganguly, A.; Sharma, S.; Papakonstantinou, P.; Hamilton, J. Probing the thermal deoxygenation of graphene oxide using high-resolution in situ X-ray-based spectroscopies. *J. Phys. Chem. C* **2011**, *115*, 17009−17019.
(47) Kozlowski, C.; Sherwood, P. M. A. X-ray photoelectron-spectroscopic studies of carbon-fibre surfaces. Part 5.—The effect of pH on surface oxidation. *J. Chem. Soc. Faraday Trans.* **1985**, *81*, 2745−2756.
(48) Stohr, J. *NEXAFS Spectroscopy*; Springer-Verlag: Berlin, 1991.
(49) Pacilé, D.; Papagno, M.; Rodríguez, A. F.; Grioni, M.; Papagno, L.; Girit, C.; Meyer, G. C.; Begtrup, G. E.; Zettl, A. Near-edge X-ray absorption fine-structure investigation of graphene. *Phys. Rev. Lett.* **2008**, *101*, 066806.
(50) Lee, V.; Whittaker, L.; Jaye, C.; Baroudi, K. M.; Fischer, D. A.; Banerjee, S. Large-area chemically modified graphene films: electrophoretic deposition and characteriza- tion by soft X-ray absorption spectroscopy. *Chem. Mater.* **2009**, *21*, 3905−3916.
(51) Kuznetsova, A.; Popova, I.; Yates, J. T.; Bronikowski, M. J.; Huffman, C. B.; Liu, J.; Smalley, R. E.; Hwu, H. H.; Chen, J. G. Oxygen-containing functional groups on single- wall carbon nanotubes: NEXAFS and vibrational spectroscopic studies. *J. Am. Chem. Soc.* **2001**, *123*, 10699−10704.
(52) Zhang, G. S.; Sun, S.; Yang, D.; Dodelet, J. P.; Sacher, E. The surface analytical characterization of carbon fibers functionalized by H_2SO_4/HNO_3 treatment. *Carbon* **2008**, *46*, 196−205.
(53) Suda, M.; Kameyama, N.; Ikegami, A.; Suzuki, M.; Kawamura, N.; Einaga, Y. Size-re- duction induced ferromagnetism and photomagnetic effects in azobenzene-thiol- passivated gold nanoparticles. *Polyhedron* **2009**, *28*, 1868−1874.
(54) Lehtinen, P. O.; Foster, A. S.; Ma, Y.; Krasheninnikov, A. V.; Nieminen, R. M. Irradiation-Induced Magnetism in Graphite: A Density Functional Study. *Phys. Rev. Lett.* **2004**, *93*, 187202−187205.
(55) Harigaya, K. The mechanism of magnetism in stacked nanographite: theoretical study. *J. Phys.: Condens. Matter* **2001**, *13*, 1295−1302.
(56) Esquinazi, P.; Spemann, D.; Höhne, R.; Setzer, A.; Han, K. H.; Butz, T. Induced Magnetic Ordering by Proton Irradiation in Graphite. *Phys. Rev. Lett.* **2003**, *91*, 227201−227204.
(57) Baghayeri, M.; Ansari, R.; Nodehi, M.; Razavipanah, I.; Veisi, H. Voltametric aptasensor for bisphenol A based on the use of a MWCNT/Fe_3O_4@gold nanocomposite. *Microchim. Acta* **2018**, *185* (7), 320.
(58) Aguiló-Aguayo, N.; Inestrosa-Izurieta, M. J.; García-Céspedes, J.; Bertran, E. Morphological and Magnetic Properties ofSuperparamagnetic Carbon-Coated FeNanoparticles Produced by Arc Discharge. Morphological and Magnetic Properties of Superparamagnetic Carbon-Coated Fe Nanoparticles Produced by Arc Discharge. *J. Nanosci. Nanotechnol.* **2010**, *10* (4), 2646−2649.
(59) Yazyev, O. V.; Helm, L. Defect-induced magnetism in graphene. *Phys. Rev. B* **2007**, *75*, 125408.
(60) Gabriel, S.; Lau, R. W.; Gabriel, C. The dielectric properties of biological tissues: III. Parametric models for the dielectric spectrum of tissues. *Phys. Med. Biol.* **1996**, *41*, 2271−2293.
(61) Goncalves, G.; Marques, P. A. A. P.; Granadeiro, C. M.; Nogueira, H. I. S.; Singh, M. K.; Grácio, J. Surface modification of graphene nanosheets with gold nanoparticles: The role of oxygen moieties at graphene surface on gold nucleation and growth. *Chem. Mater.* **2009**, *21*, 4796−4802.
(62) Ray, S. C.; Pao, C. W.; Chiou, J. W.; Tsai, H. M.; Jan, J. C.; Pong, W. F.; McCann, R.; Roy, S. S.; Papakonstantinou, P.; McLaughlin, J. A. Electronic properties of a-CNx thin films: An x-ray-absorption and photoemission spectroscopy study. *J. Appl. Phys.* **2005**, *98*, 033708.
(63) Ray, S. C.; Pao, C. W.; Tsai, H. M.; Chiou, J. W.; Pong, W. F.; Tsai, M. H.; Okpalugo, T. I. T.; Papakonstantinou, P.; Pi, T. W. Enhancement of sp^3-bonding in high-bias-voltage grown diamond-like carbon thin films studied by x-ray absorption and photoemission spectroscopy. *J. Phys.: Condens. Matter* **2007**, *19*, 176204.
(64) Ray, S. C.; Pao, C. W.; Tsai, H. M.; Bose, B.; Chiou, J. W.; Pong, W. F.; DasGupta, D. Orientation of graphitic planes during annealing of "dip depos- ited" amorphous carbon film: A carbon K-edge X-ray absorption near-edge study. *Carbon* **2006**, *44*, 1982−1985.
(65) Carmeli, I.; Skakalova, V.; Naaman, R.; Vager, Z. Magnetization of Chiral Monolayers of Polypeptide: A Possible Source of Magnetism in Some Biological Membranes We are grateful to Prof. M. Fridkin and his group for helping us in the synthesis of the polyalanine. Partial support from the US−Israel Binational Science Foundation is acknowledged. *Angew. Chem., Int. Ed. Engl.* **2002**, *41*, 761−764.
(66) Tang, T.; Liu, F.; Liu, Y.; Li, X.; Xu, Q.; Feng, Q.; Tang, N.; Du, Y. Identifying the magnetic properties of graphene oxide. *Appl. Phys. Lett.* **2014**, *104*, 123104.
(67) Lee, J.; Novoselov, K. S.; Shin, H. S. Interaction between Metal and Graphene: Dependence on the Layer Number of Graphene. *ACS Nano* **2010**, *5*, 608−612.
(68) Chen, R.; Das, S. R.; Jeong, C.; Khan, M. R.; Janes, D. B.; Alam, M. A. Co-percolating graphene-wrapped silver nanowire network for high performance, highly stable, transparent conducting electrodes. *Adv. Funct. Mater.* **2013**, *23*, 5150−5158.

https://doi.org/10.1021/acsomega.4c05962
ACS Omega 2024, 9, 40067−40074